Printed in the Republic of Korea

ANALYTICAL SCIENCE & TECHNOLOGY

Vol. 39 No. 2, 105-113, 2026

https://doi.org/10.5806/AST.2026.39.2.105

Preparation of cobalt-decorated porous carbon nanofibers and their application as supercapacitor electrodes

Hyo Jin Cho[1,†], Mi Jin Park[1,†], Sang Eun Hong[1], Kun Cho[2], and Kuk Ro Yoon[1,★]

[1]Department of Chemistry, Hannam University, Daejeon 34054, Republic of Korea

[2]Center for Research Equipment, Korea Basic Science Institute, Cheongju 28119, Republic of Korea

(Received February 3, 2026; Revised February 11, 2026; Accepted February 11, 2026)

Abstract: Porous carbon nanofibers have attracted considerable attention as electrode materials for supercapacitors owing to their high specific surface area and excellent electrical conductivity. In this study, cobalt was introduced onto porous carbon nanofibers fabricated using calcium carbonate ($CaCO_3$) nanoparticles as sacrificial templates via an electrodeposition method, and the resulting electrochemical performance was investigated. The prepared nanofibers exhibited a porous structure, and the cobalt-decorated porous carbon nanofibers showed reduced internal resistance and enhanced specific capacitance compared to pristine porous carbon nanofibers. These results demonstrate that cobalt deposition effectively improves the energy storage performance of porous carbon nanofiber-based electrodes, suggesting their potential application as supercapacitor electrodes.

Key words: carbon nanofibers, cobalt electrodeposition, supercapacitor, energy storage

1. Introduction

Energy storage systems that address the intermittency of renewable energy sources have attracted increasing attention as sustainable energy technologies continue to develop. Supercapacitors are regarded as promising energy storage devices because they can complement conventional batteries through rapid charge–discharge capability, high power density, long cycle life, and operational safety. In contrast to batteries that rely on faradaic redox reactions, supercapacitors store energy via ion adsorption and desorption at electrode surfaces and are generally classified as electric double-layer capacitors, pseudocapacitors, or hybrid capacitors. Since electrode characteristics play a critical role in determining electrochemical performance, carbon-based materials have been extensively investigated as electrode materials due to their favorable electrical conductivity, large surface area, and cost-effectiveness.[1-4] Graphene, activated carbon, and carbon nanotubes have been widely studied as representative carbon-based electrodes for supercapacitor applications. Carbon electrodes have been developed in a variety of architectures to achieve stable charge storage performance during device operation. Graphene sheets and carbon nanotubes facilitate electron transport

[†]These authors contributed equally to this work.

★ Corresponding author

Phone : +82-(0)42-629-8826 Fax : +82-(0)42-629-8811

E-mail : kryoon@hnu.kr

while providing extensive surface exposure, leading to rapid electrochemical responses. In practical electrode fabrication, however, these materials are often processed as powders or thin films, where aggregation, insufficient mechanical cohesion, and fabrication complexity can reduce electrode reliability. These challenges have prompted the exploration of carbon architectures that maintain mechanical stability while supporting electrochemical activity. Carbon fibers mitigate several of these issues owing to their continuous and mechanically robust morphology. Electron transport occurs along the fiber axis, and the fibrous network remains structurally stable during repeated charge–discharge cycles. Carbon fibers are commonly classified according to their precursor materials, including pitch-based, rayon-based, and polyacrylonitrile (PAN)-based fibers. PAN-based carbon fibers are frequently selected because thermal treatment produces reproducible carbon frameworks with stable yields.[5] Electrospinning allows PAN to be processed into nanofibrous networks with controlled fiber dimensions and consistent connectivity. Under a high electric field, polymer solutions elongate into continuous fibers that assemble into nonwoven mats. Subsequent carbonization preserves the fibrous network while introducing electrical conductivity. This structural configuration promotes continuous electron transport and facilitates electrolyte ion access to active surfaces, rendering electrospun carbon nanofibers suitable for electrode applications.[6] In many cases, enhancing electrochemical performance requires additional modification beyond control of fiber morphology. Porosity has often been introduced using sacrificial templates to increase the number of accessible ion adsorption sites. Alternatively, transition metals including cobalt, nickel, and manganese have been incorporated to promote surface redox reactions.[7,8] In many previous studies, these modifications are performed during precursor synthesis or carbonization. As a result, changes in structure, electrical properties, and surface chemistry occur concurrently, making it difficult to isolate interfacial contributions to electrochemical performance. Electrodeposition provides a practical approach to decouple these effects. Because deposition occurs after formation of the carbon framework, metal species can be introduced selectively at the electrode surface while preserving the underlying structure.[9,10] Despite this advantage, electrodeposition has rarely been combined with template-derived porous carbon nanofibers in studies focused on interfacial charge transport rather than dominant pseudocapacitive behavior.[11] In this study, PAN nanofibers were prepared by electrospinning and converted into carbon nanofibers through carbonization. Calcium carbonate nanoparticles were used to introduce porosity within the fibrous structure. Cobalt deposition was then carried out as a separate step using electrodeposition. This sequential processing scheme enables independent control over pore formation and metal incorporation. The electrochemical behavior of the resulting cobalt-decorated porous carbon nanofibers was investigated to evaluate the impact of interfacial modification on charge storage behavior in supercapacitor electrodes.

2. Experimental

2.1. Materials

Polyacrylonitrile (PAN, powder, Mw ≈ 85,000) was purchased from Goodfellow (UK). Calcium chloride anhydrous (96.0 %) and tetrahydrofuran (THF, 99.5 %) were obtained from SAMCHUN (Republic of Korea). Sodium carbonate (≥99.5 %, ACS reagent), N,N-dimethylformamide (DMF, anhydrous, 99.8 %), 1-butanol (anhydrous, 99.8 %), cetyltrimethylammonium bromide (CTAB), hexane (anhydrous, 95 %), and ethyl alcohol (99.5 %) were purchased from Sigma-Aldrich (USA). Cobalt(II) nitrate hexahydrate (99 %, pure) was supplied by ACROS Organics (Belgium). Hydrochloric acid (35 %) was obtained from Daejung (Republic of Korea), and potassium hydroxide (KOH, 95 %, flake) was purchased from OCI Company Ltd. (Republic of Korea). All chemicals were used as received without further purification.

2.2. Instrumentation

The rotary evaporator (R-200) was obtained from BUCHI (Switzerland), and the centrifuge (FLETA5) was purchased from Hanil (Republic of Korea). Electrospinning was performed using an electrospinning

system (ESR200R2D, NanoNC, Republic of Korea). Carbonization was carried out in a furnace (AJ-MBT4, Ajeon Heating Industrial, Republic of Korea). Electrochemical measurements were conducted using a potentiostat/galvanostat (PGSTAT128N, Autolab, Netherlands). A vacuum oven (VO-10X, Jeio Tech, Republic of Korea) was used for drying processes. The morphology of the samples was analyzed using field-emission scanning electron microscopy (FE-SEM, S-4800, Hitachi, Japan) and transmission electron microscopy (TEM, JEM-2100F HR, JEOL, Japan). Fourier transform infrared (FT-IR) spectra were obtained using an attenuated total reflection FT-IR spectrometer (Nicolet iS10, Thermo Scientific, USA). Particle size distribution was analyzed by dynamic light scattering (DLS, ELSZ-2000, Otsuka Electronics, Japan), and crystallographic structures were examined using X-ray diffraction (XRD, SmartLab, Rigaku, Japan).

2.3. Synthesis of calcium carbonate nanoparticles

Calcium carbonate nanoparticles ($CaCO_3$ NPs) were synthesized by referring to a previously reported method with slight modifications.[12] Cetyltrimethylammonium bromide (CTAB, 2.046 g) was dissolved in 1-butanol (5 mL) to prepare an emulsifier solution, which was subsequently added to n-hexane (17.25 mL) under stirring. While maintaining continuous stirring at 1000 rpm, an aqueous solution of $CaCl_2$ (0.1 mL, 2.0 M) and an aqueous solution of Na_2CO_3 (0.1 mL, 2.0 M) were sequentially added to the emulsifier solution. The resulting mixture was reacted at 40 °C for 30 min and then aged for 24 h at room temperature. After completion of the reaction, the precipitated products were collected by centrifugation at 15,000 rpm. The obtained precipitates were washed three times with 1-butanol and ethanol, respectively. Finally, the product was concentrated using a rotary evaporator at 70 °C and dried in a vacuum oven at 60 °C for 24 h to obtain $CaCO_3$ NPs in powder form.

2.4. Electrospinning of PAN/$CaCO_3$ nanofibers

Polyacrylonitrile (PAN) nanofibers embedded with calcium carbonate nanoparticles ($CaCO_3$ NPs) were prepared using an electrospinning technique.[13] $CaCO_3$ NPs (0.15 g) were first dispersed in a mixed solvent of N,N-dimethylformamide (DMF) and tetrahydrofuran (THF) by ultrasonication. Subsequently, PAN (0.4 g) was added to the dispersion and completely dissolved. The total amount of the DMF/THF mixed solvent was 5.6 g, with a weight ratio of 3:1 (DMF:THF). After stirring the solution for 12 h to obtain a homogeneous spinning solution, electrospinning was carried out under the conditions listed in *Table* 1. As a result, PAN/$CaCO_3$ nanofibers in the form of sheets, with $CaCO_3$ nanoparticles embedded within the fibers, were successfully obtained.

Table 1. Electrospinning condition of PAN/$CaCO_3$ nanofibers

Electrospinning conditions	
Flow rate	1.0 mL/h
Voltage	13 kV
Distance	10 cm
Gauge	18 G
Temperature	Room temperature

2.5. Carbonization-induced formation of porous carbon nanofibers

Porous carbon nanofibers (PCNFs) were prepared using PAN nanofibers as precursors and calcium carbonate ($CaCO_3$) nanoparticles as sacrificial templates.[13] The as-prepared PAN/$CaCO_3$ nanofibers were carbonized by heating to 800 °C at a ramping rate of 2 °C min^{-1} under a nitrogen atmosphere and maintained at this temperature for 2 h. After carbonization, the samples were cooled to room temperature under nitrogen, yielding carbon nanofibers embedded with CaO nanoparticles. To remove the CaO templates, the carbonized nanofibers were treated with an aqueous HCl solution (1.5 M) for 1 h, followed by thorough washing with deionized water and ethanol to remove residual acid. The resulting porous carbon nanofibers were then dried in an oven at 60 °C.

2.6. Electrodeposition of cobalt on porous carbon nanofibers

Cobalt-decorated porous carbon nanofibers (Co-

PCNFs) were prepared by electrodeposition of cobalt ions onto the surface of porous carbon nanofibers.[14] An aqueous electrolyte solution of cobalt(II) nitrate hexahydrate ($Co(NO_3)_2 \cdot 6H_2O$, 0.01 M) was prepared at room temperature. Electrodeposition was carried out using a three-electrode system, in which an Ag/AgCl electrode served as the reference electrode, a platinum electrode as the counter electrode, and the previously dried porous carbon nanofibers as the working electrode. Electrodeposition was conducted potentiostatically by applying a constant cathodic potential of -1.0 V versus Ag/AgCl for 300 s using a potentiostat/galvanostat, and the deposition process was repeated three times to ensure sufficient cobalt loading. As a result, cobalt species were successfully deposited onto the surface of the porous carbon nanofibers.

2.7. Electrochemical performance evaluation

The electrochemical performance of the prepared samples was evaluated using a potentiostat/galvanostat (PGSTAT128N, Autolab). All electrochemical measurements, including cyclic voltammetry (CV), electrochemical impedance spectroscopy (EIS), and galvanostatic charge-discharge (GCD) tests, were conducted in a two-electrode configuration using 6 M KOH aqueous electrolyte. Two identical electrodes were prepared by cutting the cobalt-decorated porous carbon nanofibers, and a filter paper was used as a separator between the electrodes. The specific capacitance was calculated from the GCD curves according to the equation $C = (I \times \Delta t) / (m \times \Delta V)$, where C is the specific capacitance (F g^{-1}), I is the discharge current (A), Δt is the discharge time (s), ΔV is the potential window during the discharge process (V), and m is the mass of a single electrode (g). The mass loading of each electrode was fixed at 1 mg.

3. Results and Discussion

3.1. FT-IR spectra of PAN/$CaCO_3$ and porous carbon nanofibers

FT-IR spectra were measured for pristine PCNFs and cobalt-decorated PCNFs to examine surface functional groups before and after cobalt deposition. Both samples exhibit absorption features typically observed in carbon nanofiber materials, indicating that the carbon framework is maintained following the electrodeposition process. A broad absorption band appears near 3,400 cm^{-1} in both spectra, which is associated with O–H stretching vibrations originating from surface hydroxyl groups and adsorbed moisture. An absorption band located around 1,630 cm^{-1} is observed for both samples and is assigned to C=C stretching vibrations within graphitic carbon domains. Several absorption features related to C–O-containing functionalities are detected in the lower wavenumber region. Bands appearing between 1,410 and 1,490 cm^{-1} correspond to asymmetric stretching vibrations of

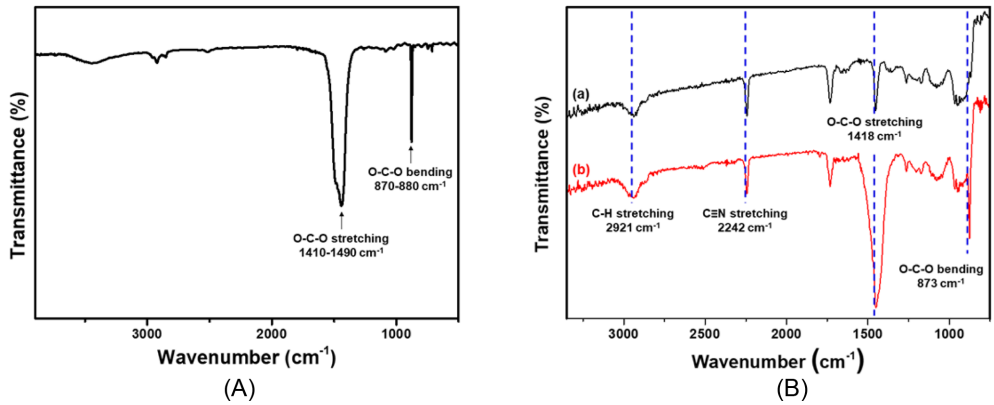

Fig. 1. FT-IR spectra of (A) $CaCO_3$ nanoparticles, (B) PAN nanofibers (a) and PAN/$CaCO_3$ nanofibers (b).

O–C–O groups. Additional bands observed in the ranges of 870–880 cm^{-1} and weak absorption features in the range of 710–750 cm^{-1} are attributed to out-of-plane and in-plane bending modes of O–C–O bonds, respectively. These features suggest the presence of residual oxygen-containing functional groups on the carbon surface, which may originate from carbonate-related species associated with the pore-forming process.

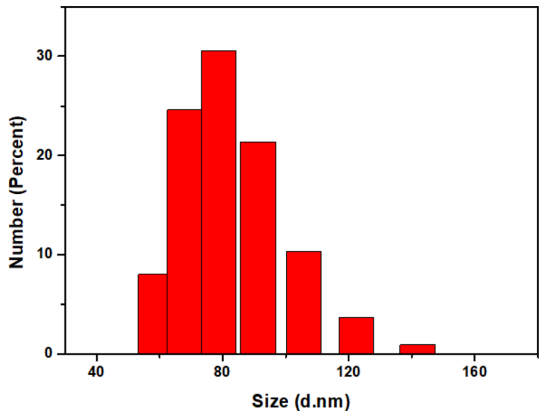

Fig. 2. DLS of $CaCO_3$ nanoparticles.

3.2. Particle size distribution measured by DLS

The hydrodynamic size distribution of the synthesized $CaCO_3$ nanoparticles was analyzed by dynamic light scattering (DLS) (*Fig.* 2). For the measurements, the nanoparticles were dispersed in ethanol at a concentration of 10 μM and sonicated for 30 min with intermittent cycles (3 min on/off) prior to analysis. The refractive index of the dispersant was set to 1.3. The DLS results show that the hydrodynamic diameters of the $CaCO_3$ nanoparticles are mainly distributed in the range of approximately 60–120 nm. This size range is larger than the primary particle size (~50 nm) observed in TEM images, which can be attributed to the formation of small aggregates in the dispersion and the intrinsic difference between hydrodynamic diameters measured by DLS and dry-state particle sizes obtained from TEM. The hydrodynamic diameter reflects not only the solid particle core but also solvent-associated layers and loosely bound aggregates present in the liquid phase. The particle size distribution in this study is presented in a number-weighted format, which provides a representative description of the

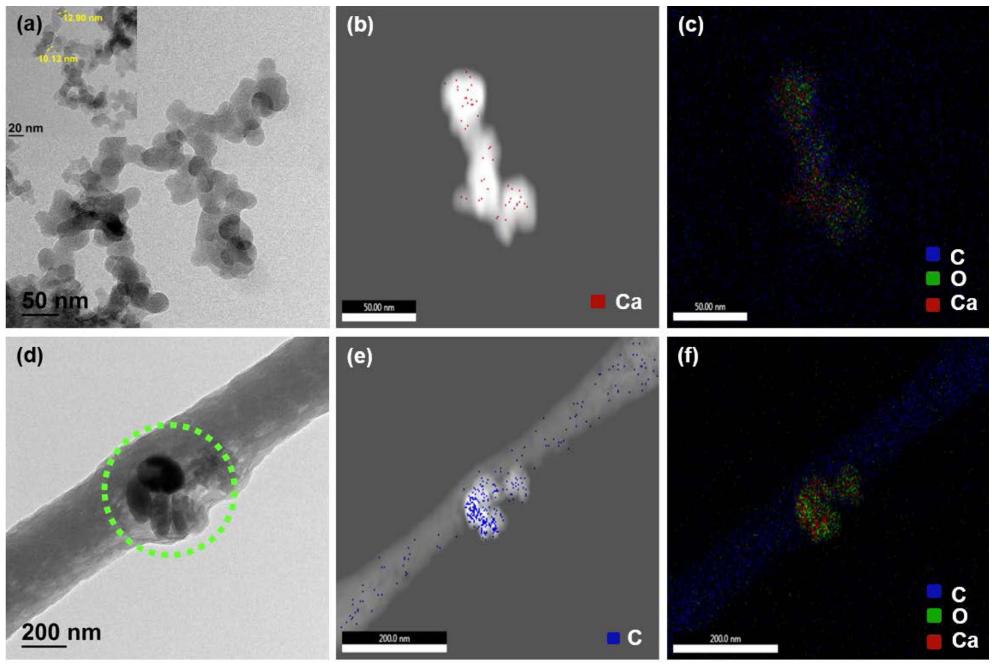

Fig. 3. TEM images of $CaCO_3$ NPs (a) and PAN/$CaCO_3$ NFs (b) STEM-EDS mapping images of $CaCO_3$ NPs (c-d) and PAN/$CaCO_3$ NFs (e-f).

dominant particle population and reduces the influence of larger aggregates that can be overemphasized in intensity-weighted distributions. Despite sonication treatment, a minor degree of aggregation cannot be completely excluded, contributing to the observed distribution width.

3.3. Morphology and structure observed by FE-TEM

The morphology of $CaCO_3$ nanoparticles and their incorporation into PAN nanofibers were examined by FE-TEM (*Fig.* 3). The $CaCO_3$ nanoparticles exhibited particle sizes below 50 nm with predominantly quasi-spherical morphology. Due to the small primary particle size, the nanoparticles appeared as nanoscale domains. Elemental analysis by EDS revealed the presence of calcium (20 wt%), carbon (57 wt%), and oxygen (23 wt%), which is consistent with the stoichiometric composition of $CaCO_3$. TEM images of PAN/$CaCO_3$ nanofibers showed that $CaCO_3$ nanoparticles were embedded within the nanofiber matrix and distributed as nanoscale domains along the fibers. EDS elemental mapping further confirmed the coexistence of carbon from PAN and calcium and oxygen from $CaCO_3$, demonstrating the successful incorporation of $CaCO_3$ nanoparticles into the PAN nanofibers.

3.4. Surface morphology of nanofibers revealed by FE-SEM

The morphological evolution of the nanofibers was investigated by FE-SEM for pristine PAN nanofibers, PAN/$CaCO_3$ nanofibers, porous carbon nanofibers (PCNFs), and cobalt-decorated PCNFs (*Fig.* 4). Pristine PAN nanofibers exhibited a continuous and uniform fibrous morphology without bead formation, with an average diameter of approximately 500 nm. PAN/$CaCO_3$ nanofibers also maintained a fibrous structure;

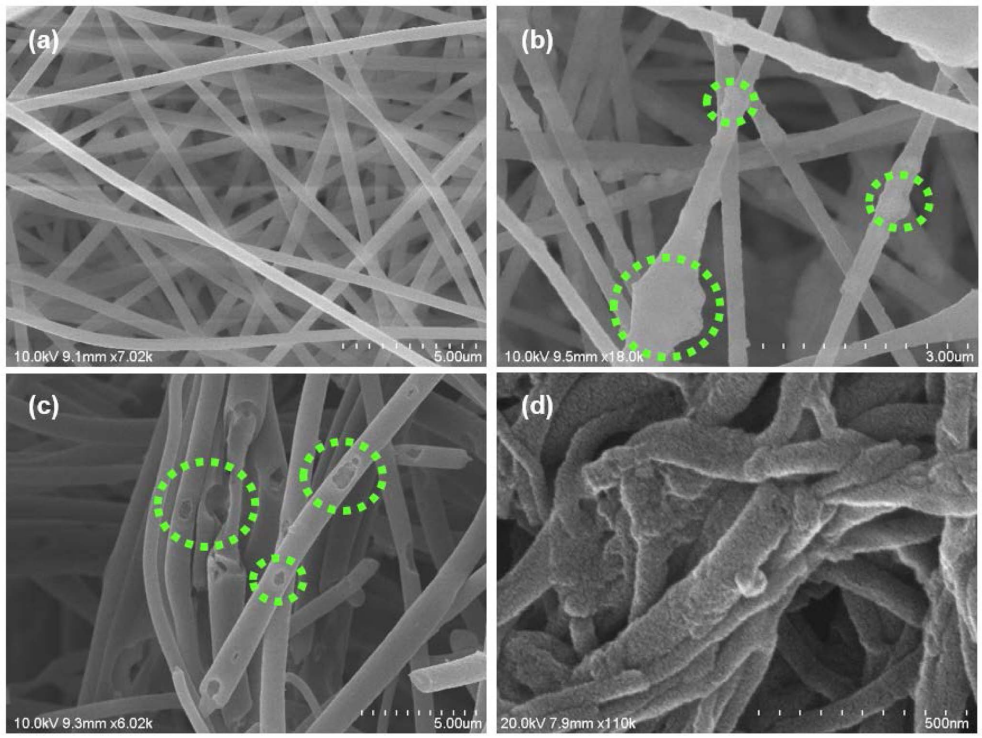

Fig. 4. FE-SEM images of (a) PAN NFs, (b) PAN NFs embedded $CaCO_3$ NPs (green circles are embedded $CaCO_3$ NPs), (c) PCNFs removing $CaCO_3$ NPs after carbonization of PAN/$CaCO_3$ NFs (green circles are the pore in which NPs were removed), and (d) cobalt-decorated PCNFs.

however, localized irregular regions were observed along the fibers. These regions are associated with the presence of $CaCO_3$ nanoparticles embedded in the polymer matrix. In addition, $CaCO_3$ nanoparticles were not uniformly dispersed but appeared as clustered domains, reflecting partial aggregation within the fibers. After carbonization and subsequent removal of $CaCO_3$ nanoparticles, the resulting PCNFs preserved the overall fibrous morphology, although partial fiber breakage was observed as a result of high-temperature treatment. Irregular pore structures were generated within the fibers, which is related to the non-uniform size and shape of the $CaCO_3$ sacrificial templates. In the case of cobalt-decorated PCNFs, the fiber surfaces became rougher, and the pore structures were less clearly distinguished compared with pristine PCNFs. This morphological change implies that cobalt species were deposited on the external surface of the fibers and also partially within the porous structure formed after template removal.

3.5. Elemental composition analyzed by EDS

EDS analysis was performed to verify the elemental composition of PCNFs and cobalt-decorated PCNFs (*Fig.* 5). The EDS spectrum of PCNFs is dominated by carbon signals, while calcium and oxygen originating from $CaCO_3$ nanoparticles are not detected, indicating that the template particles were effectively removed to form porous structures. A minor chlorine signal is observed, which is likely due to residual hydrochloric acid used during the template removal process. For cobalt-decorated PCNFs, both carbon and cobalt signals are detected with a weight ratio of approximately 89 % and 11 %, respectively. This result confirms the successful deposition of cobalt onto the porous carbon nanofibers via the electrodeposition process.

3.6. Electrochemical performance

The electrochemical performance of pristine PCNFs and cobalt-decorated PCNFs was evaluated using cyclic voltammetry, electrochemical impedance spectroscopy, and galvanostatic charge–discharge measurements under identical conditions. Cobalt-decorated PCNFs exhibit a larger enclosed area in cyclic voltammograms compared with pristine PCNFs within the same potential window, indicating an increase in stored charge. Over scan rates ranging from 5 to 100 mV s^{-1}, the overall shape of the voltammograms is largely preserved, while minor distortions appear at higher scan rates, which is commonly observed for porous carbon electrodes under kinetic limitations. Electrochemical impedance spectra reveal notable differences in interfacial resistance between the two electrodes. The real-axis intercept decreases from approximately 15–16 Ω for pristine PCNFs to 2–3 Ω for cobalt-decorated PCNFs, reflecting a reduction in

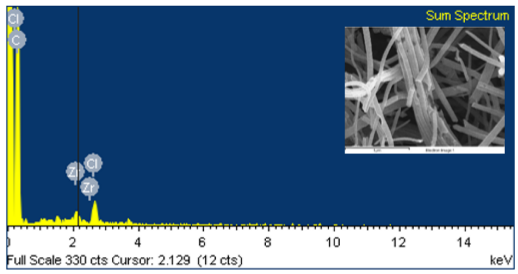

Element	Weight%	Atomic%
C K	93.55	98.29
Cl K	3.74	1.33
Zr L	2.71	0.38
Totals	100.00	

(a)

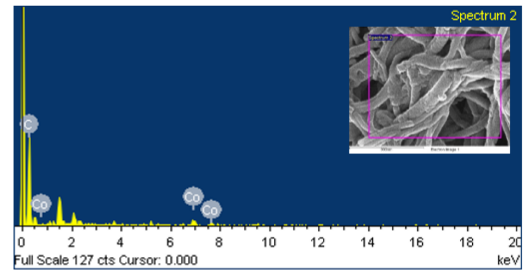

Element	Weight%	Atomic%
C K	88.73	97.48
Co K	11.27	2.52
Totals	100.00	

(b)

Fig. 5. SEM-EDS of (a) PCNFs and (b) cobalt-decorated PCNFs.

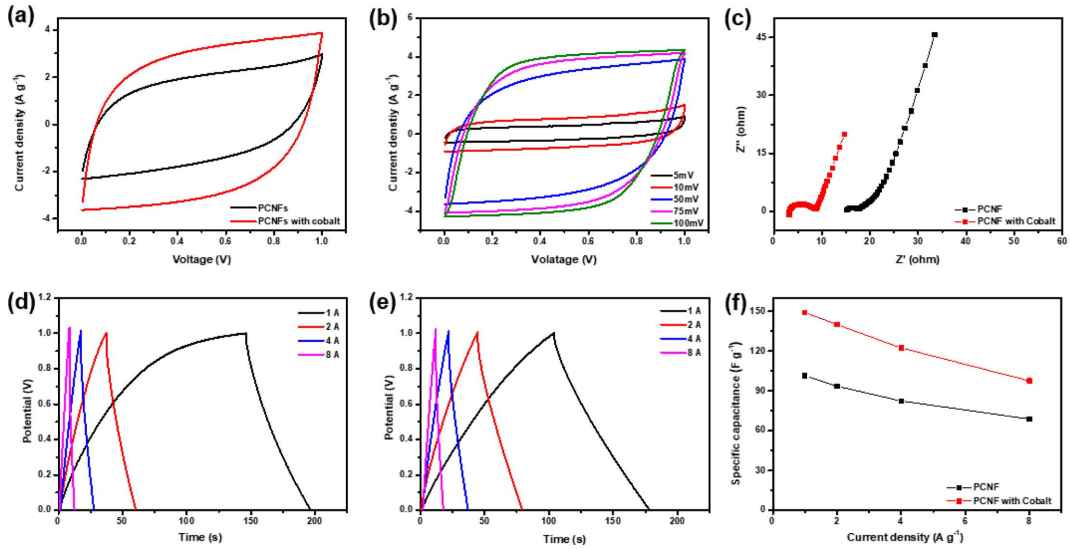

Fig. 6. Electrochemical performance of PCNFs and cobalt-decorated PCNFs measured in 6 M KOH electrolyte: (a) CV curves of PCNFs and cobalt-decorated PCNFs at 50 mV s^{-1}, (b) CV curves of cobalt-decorated PCNFs at different scan rates, (c) EIS curves of PCNFs and cobalt-decorated PCNFs, (d), (e) GCD curves of PCNFs and cobalt-decorated PCNFs, (f) specific capacitances of PCNFs and cobalt-decorated PCNFs.

equivalent series resistance. In addition, the diameter of the semicircle in the medium-frequency region becomes smaller after cobalt deposition, indicating decreased charge-transfer resistance at the electrode–electrolyte interface. These changes in interfacial resistance are reflected in galvanostatic charge–discharge behavior. Pristine PCNFs show a pronounced IR drop and deviation from linear discharge profiles, whereas cobalt-decorated PCNFs exhibit reduced IR drop and more symmetric charge–discharge curves at identical current densities. The specific capacitance increases from approximately 101 F g^{-1} for pristine PCNFs to 148 F g^{-1} for cobalt-decorated PCNFs at a current density of 1 A g^{-1}. At higher current densities of 2, 4, and 8 A g^{-1}, cobalt-decorated PCNFs deliver capacitance values of approximately 139, 121, and 97 F g^{-1}, respectively, while pristine PCNFs show values of approximately 93, 82, and 68 F g^{-1}. Despite the increase in specific capacitance, both electrodes exhibit comparable trends in capacitance retention with increasing current density. This behavior suggests that cobalt deposition primarily enhances electrochemical performance through reduced interfacial resistance and improved charge-transfer kinetics, while the overall charge storage mechanism remains dominated by electric double-layer capacitance.

4. Conclusions

Porous carbon nanofibers were produced from electrospun PAN/$CaCO_3$ composite nanofibers by carbonization and subsequent removal of the $CaCO_3$ templates. Structural and compositional analyses confirmed the formation of a porous carbon framework associated with the sacrificial $CaCO_3$ phase. Cobalt was introduced onto the porous carbon nanofibers by an electrodeposition process. Microscopic observation and elemental analysis showed that cobalt species were present on the fiber surface and within the pore regions formed after template removal. Electrochemical measurements showed differences in charge storage behavior between pristine and cobalt-deposited porous carbon nanofibers. The specific capacitance increased from approximately 101 to 148 F g^{-1} at a current density of 1 A g^{-1} after cobalt deposition. At current densities of 2, 4, and 8 A g^{-1}, the cobalt-deposited electrodes exhibited specific capacitances of approximately 139, 121, and 97 F g^{-1}, respectively, while

the pristine electrodes exhibited values of approximately 93, 82, and 68 F g^{-1}. The capacitance retention over the examined current-density range remained similar for both electrodes, with values of about 66–67 %. Impedance analysis showed a decrease in the real-axis intercept and a reduction in the semicircle diameter in the Nyquist plots of cobalt-deposited porous carbon nanofibers compared with pristine samples. These changes correspond to a modification of the interfacial resistance after electrodeposition. Electrodeposition modifies both the surface composition and the interfacial properties of porous carbon nanofibers. The result of electrochemical behavior can be considered in the development of porous carbon-based electrodes operated in aqueous electrolyte environments.

Acknowledgements

This work was supported by the Regional Innovation System & Education (RISE) Program through the Daejeon RISE Center, funded by the Ministry of Education (MOE) and Daejeon Metropolitan City, Republic of Korea (2026-RISE-06-013); the 2025 Hannam University Research Fund; and the National Research Foundation of Korea (NRF) grants funded by the Korean government (RS-2025-25462803 and RS-2025-25399697).

References

1. N. Kumar, Y. C. Yu, Y. H. Lu, and T. Y. Tseng, *J. Mater. Sci.*, **51**, 2320-2329 (2016). https://doi.org/10.1007/s10853-015-9540-9
2. P. Tang, L. Han, and L. Zhang, *ACS Appl. Mater. Interfaces*, **6**(13), 10506-10515 (2014). https://doi.org/10.1021/am5021028
3. A. González, E. Goikolea, J. A. Barrena, and R. Mysyk, *Renewable and Sustainable Energy Reviews*, **58**, 1189-1206 (2016). https://doi.org/10.1016/j.rser.2015.12.249
4. W. Raza, F. Ali, N. Raza, Y. Luo, K. H. Kim, J. Yang, S. Kumar, A. Mehmood, and E. E. Kwon, *Nano Energy*, **52**, 441-473 (2018). https://doi.org/10.1016/j.nanoen.2018.08.013
5. M. K. Seo and S. J. Park, *Polym. Sci. Technol.*, **21**(2), 130-140 (2010). https://koreascience.kr/article/JAKO201027463258901.view
6. H. J. Lee, J. S. Won, S. C. Lim, T. Lee, J. Y. Yoon, and S. G. Lee, *Text. Sci. Eng*., **53**(2), 103-108 (2016). https://www.kci.go.kr/kciportal/ci/sereArticleSearch/ciSereArtiView.kci?sereArticleSearchBean.artiId=ART002101965
7. S.J. Park, J.M. Rhee, H.J. Kim, S.H. Im, and S.Y. Park, *J. Korean Ind. Eng. Chem*., **18**(3), 205-212 (2007). https://www.kci.go.kr/kciportal/ci/sereArticleSearch/ciSereArtiView.kci?sereArticleSearchBean.artiId=ART001188688
8. M. Inagaki, Y. Yang, and F. Kang, *Adv. Mater.*, **24**(19), 2547-2566 (2012). https://doi.org/10.1002/adma.201104940
9. J. Ao, R. Xu, Y. Zhang, S. Feng, C. Chen, and L. Jiang, *Int. J. Electrochem. Sci.*,**16**(4), 210422 (2021). https://doi.org/10.20964/2021.04.12
10. A. Zhang, Y. Xiao, Y. Cao, H. Fang, Y. Zhang, P. Das, and H. Zhang, *J. Solid State Electrochem.*, **25**, 1503-1512 (2021). https://doi.org/10.1007/s10008-021-04929-7
11. S. A. Lee, J.W. Yang, S. K. Choi, and H. W. Jang, *Exploration*, **1**(3), 20210012 (2021). https://doi.org/10.1002/EXP.20210012
12. H. Li, X. Zhang, X. Lin, S. Zhuangm, Y. Wu, Z. Liu, J. Rong, and J. Zhao, *J. Mater. Chem. B*, **8**(6), 1223-1234 (2020). https://doi.org/10.1039/C9TB02684C
13. L. Zhang, Y. Jiang, L. Wang, C. Zhang, and S. Liu, *Electrochimica Acta*, **196**, 189-196 (2016). https://doi.org/10.1016/j.electacta.2016.02.050
14. P. T. Babar, A. C. Lokhande, B. S. Pawar, M. G. Gang, E. J. Jo, C. S. Go, M. P. Suryawanshi, S. M. Pawar, and J. H. Kim, *Applied Surface Science*, **427**(A), 253-259 (2018). https://doi.org/10.1016/j.apsusc.2017.07.142